

Chlorine-Enabled Electron Doping in Solution-Synthesised SnSe Thermoelectric Nanomaterials

Guang Han,^[a] Srinivas R. Popuri,^[b] Heather F. Greer,^[c] Lourdes F. Llin,^[d] Jan-Willem G. Bos,^[b] Wuzong Zhou,^[c] Douglas J. Paul,^[d] Hervé Ménard,^[e] Andrew R. Knox,^[d] Andrea Montecucco,^[d] Jonathan Siviter,^[d] Elena A. Man,^[d] Wen-guang Li,^[d] Manosh C. Paul,^[d] Min Gao,^[f] Tracy Sweet,^[f] Robert Freer,^[g] Feridoon Azough,^[g] Hasan Baig,^[h] Tapas K. Mallick,^[h] and Duncan H. Gregory*^[a]

Doping plays a vital role in modifying the electronic properties of semiconductors and is pivotal for (opto)electronics,^[1] photovoltaics (PV)^[2] and thermoelectrics.^[3] Metal chalcogenides (MCs) form a diversity of functional materials well-suited to such applications. Halogen doping in MCs has proven effective to realise n-type conducting behaviour and tune carrier concentrations.^[2-4] Enhanced thermoelectric and PV performance can result.^[2-4] While halogens can be readily doped into bulk MCs by high-temperature synthesis using metal halide precursors,^[4] doping proves challenging for solution-synthesised MC nanostructures.^[5] Recently, post-synthesis halide treatment of nanocrystals in solution has been developed which involves switching halogens for long chain surfactant molecules absorbed on the surface.^[2, 6] In fact, sorption of halogens can be realised as part of a one-pot synthesis using metal halide precursors.^[7] Although this strategy was initially developed for passivation of MC quantum dots against oxidation,^[2, 6-7] annealing or hot pressing halogen-coated nanoparticles allows halides to diffuse into the MC lattice and substitute for chalcogenide anions.^[8] However, controlling doping levels is not straightforward and such methods can introduce rather high halide concentrations in small nanocrystals leading to reduced electrical conductivity.^[8b]

Hence exerting control over dopant concentration without sacrificing electrical performance is imperative.

Thermoelectrics realise direct inter-conversion between thermal and electric energy, thus providing an important route to produce useful electricity from waste heat and to perform refrigeration (via the Seebeck and Peltier effects respectively).^[9] SnSe is a layer-structured MC semiconductor and potentially useful thermoelectric material given its excellent energy conversion efficiency, relatively low toxicity and the high Earth-abundance of the component elements.^[10] Most research to date has concentrated on p-type SnSe.^[10-11] Conversely n-type SnSe is difficult to achieve; only I and BiCl₃ have been used successfully to dope bulk SnSe with electrons. Moreover, high-temperature, energy-intensive processes are needed to achieve this.^[12] There are no reports of solution-synthesised SnSe nanostructures with tunable n-type conducting behaviour. Before the potential of SnSe can be fully realised, it is critical to develop a cost-effective and large-scale synthesis of high performing n-type SnSe, to complement existing p-type materials.

In this study, we demonstrate the introduction of Cl to SnSe nanoparticles by a one-pot *in-situ* solution approach to prepare > 10 g of doped SnSe nanoparticles on short timescales (Scheme 1; Figure S1). The strategy exploits the nucleophilic nature of the halide anion and the electrophilicity of coordinatively unsaturated metal cations at the nanoparticle surface,^[6] coupled with the acidic conditions that promote the formation of metal-halide bonds by ligand replacement.^[8a] The simple solution synthesis is achieved, using aqueous SnCl₂ both as reactant and Cl source and citric acid both as surfactant to restrict particle growth and means to control pH. Controlling the reaction duration allows us to engineer nanoparticle size and regulate the Cl dopant level. The nanoparticles can be hot-pressed into Cl-doped SnSe dense pellets with controllable dopant concentration and consistent n-type conducting behaviour.

[a] Dr. G. Han, Prof. D. H. Gregory
WestCHEM, School of Chemistry, University of Glasgow, Glasgow,
G12 8QQ, UK
E-mail: Duncan.Gregory@glasgow.ac.uk

[b] Dr. S. R. Popuri, Dr. J.-W. G. Bos
Institute of Chemical Sciences and Centre for Advanced Energy
Storage and Recovery, School of Engineering and Physical
Sciences, Heriot-Watt University, Edinburgh, EH14 4AS, UK

[c] Dr. H. F. Greer, Prof. W. Z. Zhou
EaStCHEM, School of Chemistry, University of St Andrews,
St Andrews, Fife KY16 9ST, UK

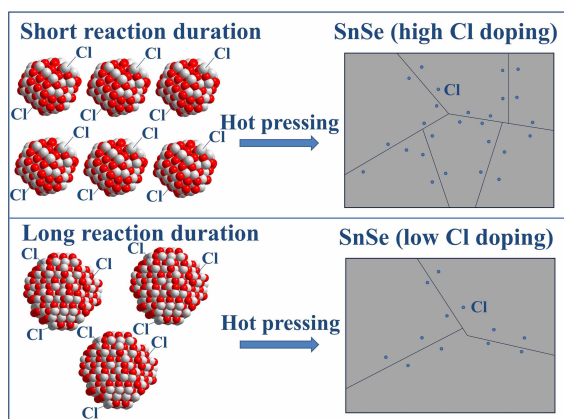
[d] Dr. L. F. Llin, Prof. D. J. Paul, Prof. A. R. Knox, Dr. A. Montecucco,
Dr. J. Siviter, Dr. E. A. Man, Dr. W.-g. Li, Dr. M. C. Paul
School of Engineering, University of Glasgow, Glasgow, G12 8QQ,
UK

[e] Dr. H. Ménard
Sasol (UK) Ltd, St Andrews, KY16 9ST, UK

[f] Prof. M. Gao, Dr. T. Sweet
School of Engineering, Cardiff University, Cardiff, CF24 3AA, UK

[g] Prof. R. Freer, Dr. F. Azough
School of Materials, University of Manchester, Manchester, M13
9PL, UK

[h] Prof. T. K. Mallick, Dr. H. Baig
Environment and Sustainability Institute, University of Exeter
Penryn Campus, Penryn TR10 9FE UK



Scheme 1. The strategy to fabricate n-type SnSe nanostructured pellets utilises Cl concentration and nanoparticle size from solution-synthesis.

Injection of a NaHSe aqueous solution into a SnCl_2 solution (26:1 molar ratio of citric acid: SnCl_2) leads to the immediate formation of an SnSe precipitate (Equation 1):



Boiling the suspension for 2 h generates crystalline, phase-pure SnSe nanoparticles. Powder X-ray diffraction (PXRD) patterns can be exclusively indexed to orthorhombic SnSe (ICDD card No. 48-1224).^[13] Rietveld refinement against PXRD data (Figure 1a; Tables S1, S2) confirms that the single phase SnSe product crystallises in orthorhombic space group $Pnma$, with $a = 11.5424(8)$ Å, $b = 4.1775(4)$ Å and $c = 4.3841(5)$ Å. Scanning electron microscopy (SEM) images (Figures S2a,b) reveal that the product is an agglomeration of nanoparticles with individual sizes of 15–55 nm. Energy dispersive X-ray spectroscopy (EDS) spectra (Figure S2c) taken across the samples as point and area scans consistently generate Sn:Se:Cl atomic ratios of 50.6(5):48.8(5):0.6(1). The existence of Cl should result from the interaction of nucleophilic Cl^- and electrophilic Sn^{2+} at the nanoparticle surface^[6] together with the replacement of ligated citric acid by Cl^- in the acidic environment during solution heating.^[8a] Transmission electron microscopy (TEM) images (Figures 1b, S2d) confirm that SnSe nanoparticles assemble into clusters with an average individual particle size of ~35 nm. Selected area electron diffraction (SAED) patterns (Figure 1b) collected from a section of such a cluster reveal the polycrystalline nature of the SnSe particles. High resolution TEM (HRTEM) images (Figure 1c) nevertheless demonstrate the single crystalline nature of individual nanoparticles. Elemental mapping (Figure 1d) confirms the existence and uniform distribution of Sn, Se and Cl in the nanoparticles.

Controlling the synthesis duration can predetermine both the particle size and Cl content of the SnSe nanoparticles. To illustrate this, we synthesised materials from 1, 5 min and 24 h of solution heating. PXRD (Figures S3, S4; Table S1) reveals each product to be single-phase with the orthorhombic SnSe structure. The refined cell volumes increase slightly with reaction time and the Bragg half-widths decrease gradually as the reaction duration increases, indicating likely crystallite growth. SEM (Figures S5a-f) and TEM (Figures 2a, 2b, S6a) images

show that the products are composed of nanoparticles, and the average particle size increases from ~25 nm through ~30 nm to ~50 nm, as heating is extended. EDS (Figures S5g-i) confirms the existence of Cl in all the samples and shows increased Cl levels for shorter reaction times; specifically, the Sn:Se:Cl atomic ratios are 48.2(5):50.5(5):1.3(2), 51.6(5):47.7(5):0.7(1) and 51.5(5):48.2(5):0.3(1) for nanoparticles synthesised after 1 min, 5 min and 24 h, respectively. SAED patterns (Figures 2a, b, S6b) confirm the polycrystalline nature of the SnSe nanoparticles. Furthermore, HRTEM (Figures 2c, S6c, d) reveals that the products synthesised after 1 and 5 min have relatively poor crystallinity, and nanoparticles with sizes of 2–4 nm are attached on the surface of larger particles. When the reaction time is increased to 2 or 24 h (Figure 2d), individual particles become single crystalline. This suggests that the aggregation and coalescence of small nanoparticles leads to the formation of larger single crystalline nanoparticles.^[14]

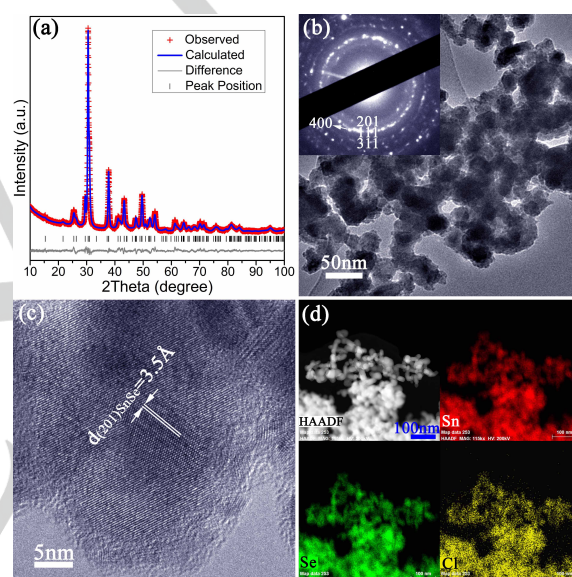


Figure 1. Characterisation of SnSe nanoparticles synthesised after 2 h: (a) Profile plot from Rietveld refinement against PXRD data; (b) TEM image and corresponding SAED pattern collected from the nanoparticles; (c) HRTEM image of an individual nanoparticle with the (201) d-spacing indicated; (d) EDS mapping of a nanoparticle cluster. The 4 panels in (d) are (clockwise from top left) high angle annular dark field (HAADF) image, elemental mapping for Sn (red), Cl (yellow) and Se (green).

The ability to prepare SnSe nanomaterials in > 10 g quantities allowed the facile fabrication of SnSe pellets via hot pressing without the variations in sample morphology that could ensue from repeated sample preparation. Pellets with ~95 % of the SnSe theoretical density, consolidated from 2 h solution-synthesised powder, were obtained (denoted 1). Rietveld refinement (Figure S7, Table S3) shows that the pellets are composed principally of orthorhombic SnSe (79.1(1) wt.%) but also of two minority phases of trigonal SnSe_2 (11.1(3) wt.%) and tetragonal SnO_2 (9.8(2) wt.%). This indicates that a small proportion of SnSe was oxidised to SnO_2 and SnSe_2 during the hot pressing process ($2\text{SnSe} + \text{O}_2 \rightarrow \text{SnO}_2 + \text{SnSe}_2$). A series of subsequent experiments (see Supporting Information; Figures S8-S15; Tables S4-S6) confirmed that the oxidation was less in nanomaterials prepared at longer reaction durations. Both

particle size (and by inference surface area) and the relative amount of surface carboxyl groups could be traced as contributors to the oxidation process.

Preferred orientation of both SnSe and SnSe₂ crystallites is evidenced by the increased intensity of the (*h*00) and (00*l*) reflections respectively in PXD patterns from the pellets (Figure S16). This suggests that the longest crystallographic axes of the respective cells align parallel to the hot pressing direction. Considering that the magnitude of the electrical conductivity is highest perpendicular to these long axes in both SnSe and SnSe₂,^[10a, 15] such an orientation should be beneficial in enhancing electrical conductivity perpendicular to the hot pressing direction of the pellets.

SEM and TEM images (Figures S17a, b, S18a) show that **1** is composed of densely packed plates with almost uniformly distributed particles. EDS (Figures S17c-g) confirms the existence and uniform distribution of Cl in **1**. SAED patterns (Figure S18b) taken from a number of plates and nanoparticles from **1** confirm the presence of the above-mentioned three phases: SnSe, SnSe₂ and SnO₂. HRTEM images demonstrate that the predominant plate-like structures in **1** are crystalline SnSe (Figure S18c). High resolution images also show that some of the smaller irregular nanoplates are formed by SnSe₂ (Figure S18d) while some nanoparticles of SnO₂ are distributed among the SnSe plates (Figure S18e). Thermogravimetric-differential thermal analysis (TG-DTA) of **1** under argon (Figure S19) shows negligible weight loss below 500 °C, but reveals that decomposition begins above this temperature and corresponds to an endothermic Se sublimation process.

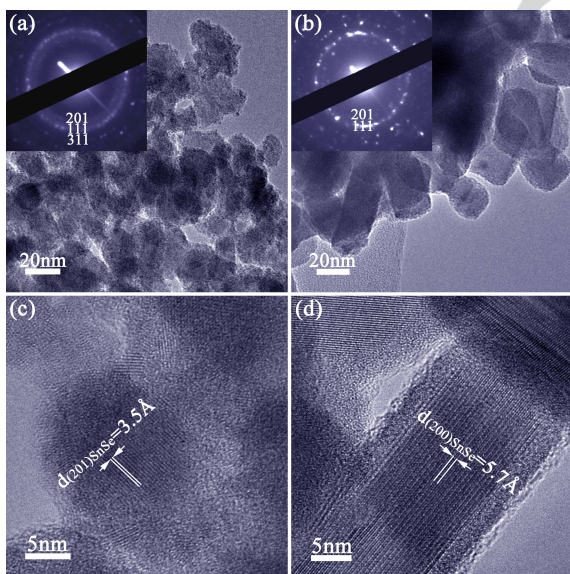


Figure 2. TEM characterisation of SnSe nanoparticles synthesised after 1 min (a, c) and 24 h (b, d): (a), (b) TEM images and corresponding SAED patterns collected from the particles; (c), (d) HRTEM images of individual nanoparticles with selected d-spacings indicated.

For comparison, the nanomaterials prepared over 1 min, 5 min and 24 h were also hot pressed into pellets (denoted **2**, **3**, **4** respectively) using the same processing parameters, achieving ~85 %, ~90 % and ~92 % of the SnSe theoretical density,

respectively. Rietveld refinement against PXD data (Figure S20; Tables S7-9) shows that the SnSe phase fraction increases from ca. 71 wt% through 72 wt% to 90 wt% for **2**, **3** and **4**, respectively, again indicating a direct correlation between synthesis time (and particle size/surface citric acid amount) and the tendency to oxidation. HRTEM on **3** confirms that SnO₂ nanoparticles are distributed in close proximity to the SnSe plates (Figure S21). EDS (Figure S22) confirms that the pellets contain Cl at levels consistent with the corresponding solution synthesised SnSe nanoparticles, suggesting no loss during the hot pressing process. X-ray photoelectron spectroscopy (XPS) was used to verify the presence of chlorine and analysis of **3** (Figure S23) shows that the peaks at 200.5 eV and 198.9 eV can be assigned to Cl 2p_{1/2} and Cl 2p_{3/2} states respectively, indicating that Cl exists in the form of Cl⁻.^[7a, 16] This implies electron doping indeed originates from the halide on substitution for Se²⁻.^[16] The indirect optical bandgap from diffuse reflectance (DR) UV-Vis spectra (Figure S24) narrows from ~0.85 through ~0.8 to ~0.75 eV, when the Cl concentration is increased from ~0.3% (**4**) through ~0.7–0.6% (**2-3**) to ~1.3% (**1**), respectively. This insinuates that the indirect bandgap of SnSe is reduced slightly but significantly by increased Cl doping. A similar bandgap narrowing was observed in I-doped SnSe and is expected to improve the electrical conductivity in SnSe.^[12a]

We selected **1**, **3** and **4** for electrical measurements due to the relatively low percentage of SnO₂ and SnSe₂ components and the high density achieved (≥ 90%). Hall measurements (Table 1) give a clear correlation between the Cl and carrier concentrations (where the majority carriers are electrons). **1** and **3** have higher carrier concentrations than **4** due to the two-fold increase in Cl content, while **3** has a lower carrier concentration than **1**, which is probably related to the higher level of impurities. The contrast in the temperature-dependent Seebeck coefficient (*S*) for the different pellets is striking (Figure 3a; Table 1). The variation in the absolute value of *S* with temperature for **1** and **3** is very similar increasing from 300 K to reach a maximum at ca. 410–425 K before decreasing by 540 K. The decreasing value of *S* at higher temperature could be due to thermal excitation of minority carriers (holes) that are related to intrinsic defects in SnSe (e.g. Sn vacancies)^[17] as manifested by the significantly enhanced electrical conductivity (Figure 3b). The absolute value of **1** is slightly lower than that of **3** at 300 K, but *S* for both **1** and **3** are negative within the whole temperature range, indicating n-type behaviour consistent with Cl doping. By comparison, **4**, with the lowest Cl doping level, shows n-type behaviour at 300 K and transforms to p-type behaviour at ~475 K with *S* ~75 μV K⁻¹ at 540 K. The n-p type transition could also be related to the thermal excitation of holes at high temperature. We also note that the impurity phases, SnSe₂ and SnO₂, are both intrinsic n-type semiconductors.^[16, 18]

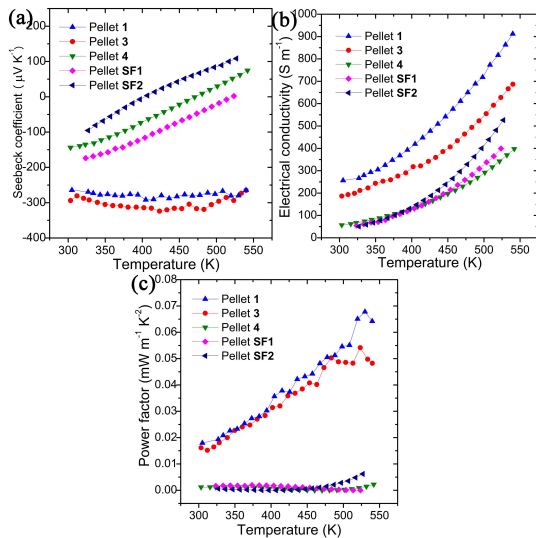


Figure 3. Electrical properties of SnSe pellets **1**, **3**, **4**, **SF1** and **SF2** measured perpendicular to the hot pressing direction: (a) the Seebeck coefficient, (b) the electrical conductivity and (c) the power factor as a function of temperature.

The electrical conductivity (σ) of **1** (Figure 3b) increases from $\sim 255 \text{ S m}^{-1}$ at 300 K to $\sim 910 \text{ S m}^{-1}$ at 540 K. With a similar Cl doping concentration and indirect bandgap to **1**, the σ of **3** is slightly lower (from $\sim 185 \text{ S m}^{-1}$ at 300 K to $\sim 685 \text{ S m}^{-1}$ at 540 K), probably due to the increase in the less conductive SnSe_2 and SnO_2 components,^[16, 18b] together with the increased carrier scattering from SnO_2 nanoparticles. This is consistent with the higher carrier concentration and mobility in **1** (Table 1). By contrast, with the lowest Cl doping level, **4** exhibits the lowest carrier concentration and σ among the three pellets, although it is the least oxidised. In fact, **1** and **3** demonstrate higher σ values than bulk I-doped SnSe materials with similar doping concentrations within the same temperature range (e.g. σ for $\text{SnSe}_{0.98}\text{I}_{0.02}$ increased from $\sim 0.23 \text{ S m}^{-1}$ at 300 K to $\sim 105 \text{ S m}^{-1}$ at 565 K) and comparable σ to Bi and Cl co-doped materials (e.g. $\text{SnSe}_{0.95}\text{-}0.2\text{mol}\% \text{BiCl}_3$ yielded σ values of $\sim 1170 \text{ S m}^{-1}$ at 300 K and $\sim 1815 \text{ S m}^{-1}$ at 560 K).^[12]

In an attempt to understand the possible origins of the n-type conducting behaviour more fully, we also measured the thermoelectric performance of two pellets synthesised using hydrochloric acid in place of citric acid (**SF1** and **SF2**; see supporting information) for comparison (Figure 3, Table 1). EDS shows that these surfactant-free samples have larger particle size and lower Cl concentrations compared to their citric acid “analogues”, **1** and **4**. (The Sn:Se:Cl ratios are 51.7(5):48.0(5):0.3(1) and 51.5(5):48.4(5):0.1(1) for **SF1** and **SF2** respectively; Figure S13). Three notable comparisons can be made: (1) **SF2** contains slightly more SnO_2 and SnSe_2 than **4** but contains less dopant Cl. **SF2** has a lower room temperature carrier concentration and σ , slightly lower magnitude Seebeck coefficient and transforms from n- to p-type at a lower temperature than **4**; (2) **SF1** has a similar Cl concentration but notably contains more SnO_2 than **4**. **SF1** transforms from n- to p-type at a higher temperature than **4**; (3) **1** and **3** remain n-type below 550 K with similar Seebeck coefficients, although the electrical conductivity of **1** is higher than **3**. Although there are

likely to be other contributing factors, the results indicate that as Cl doping levels increase so does the electrical conductivity and the temperature of the p-n transition, both observations being consistent with a higher number of negative charge carriers. Nevertheless, the presence of SnO_2 (and SnSe_2) clearly also has an effect on the electrical properties, apparently reducing the conductivity and increasing the temperature of the n-p transition. These observations would certainly be consistent with the presence of SnO_2 as a wide band gap, n-type semiconductor ($E_g = 3.6 \text{ eV}$; typically $\sigma \geq 4 \text{ S m}^{-1}$, $S \sim 200 \mu\text{V K}^{-1}$ at $\sim 300 \text{ K}$, depending on oxygen vacancy concentration).^[18] (SnSe_2 has a gap of 1.6 eV ,^[19] σ of $\sim 170 \text{ S m}^{-1}$,^[16] $S \sim 238 \mu\text{V K}^{-1}$ at $\sim 300 \text{ K}$.^[20]) Moreover, controlled doping of Cl is clearly very effective in producing high performance n-type SnSe, but oxide impurities need to be minimised to optimise this performance. It is also worth noting that the absence of surfactant in the preparation of **SF1** and **SF2** ultimately leads to significant improvements in σ , especially at higher temperature (cf. **4**).^[11d]

Table 1. A summary of Cl concentration, phase fraction, electrical properties, n-p transformation temperature, room temperature Hall carrier concentration (n_H) and mobility (μ_H) of the pellets.

Pellet	At% Cl	$S_{300\text{K}}$ [$\mu\text{V K}^{-1}$]	$\sigma_{300\text{K}}$ [S m^{-1}]	T_{n-p} [K]	Wt% SnO_2	Wt% SnSe_2	n_H [10^{18} cm^{-3}]	μ_H [$\text{cm}^2 \text{ V}^{-1} \text{ s}^{-1}$]
1	0.6(1)	-265	255	- ^[b]	9.8(2)	11.1(3)	6.43	3.60
3	0.7(1)	-295	185	- ^[b]	13.0(2)	15.3(3)	3.47	2.66
4	0.3(1)	-145	55	475	3.5(2)	6.1(2)	2.56	0.85
SF1	0.3(1)	-175 ^[a]	55 ^[a]	520	7.9(1)	6.7(2)	1.68	2.14
SF2	0.1(1)	-95 ^[a]	50 ^[a]	400	5.5(1)	6.8(2)	1.24	1.62

[a] values obtained at 325 K. [b] No transition below 550 K.

The combination of better σ values coupled with high values of S leads to higher power factors ($S^2\sigma$) in **1** ($\sim 0.018 \text{ mW m}^{-1} \text{ K}^{-2}$ at 300 K to $\sim 0.068 \text{ mW m}^{-1} \text{ K}^{-2}$ at 530 K) (Figure 3c). **3** shows slightly lower values than **1** ($S^2\sigma \sim 0.016 \text{ mW m}^{-1} \text{ K}^{-2}$ at 300 K and $\sim 0.054 \text{ mW m}^{-1} \text{ K}^{-2}$ at 525 K) as noted above. In contrast, the $S^2\sigma$ values for **4** are much lower ($\sim 0.001 \text{ mW m}^{-1} \text{ K}^{-2}$ at 300 K and reaching only $\sim 0.002 \text{ mW m}^{-1} \text{ K}^{-2}$ at 540 K). **SF1** and **SF2** achieve similar $S^2\sigma$ values at room temperature where they are both n-type, whereas **SF2** has a higher power factor at 525 K (where it is p-type). The contrast in performance between samples underscores the importance of being able to tune the degree of Cl doping and to control the pellet phase composition during fabrication. It is especially notable that the power factor for **1** compares very favourably with those for I-doped SnSe (e.g. $\text{SnSe}_{0.98}\text{I}_{0.02}$, with $S^2\sigma$ of $\sim 0.016 \text{ mW m}^{-1} \text{ K}^{-2}$ at 565 K) and co-doped SnSe (e.g. $\text{SnSe}_{0.95}\text{-}0.2\text{mol}\% \text{BiCl}_3$, with an $S^2\sigma$ of $\sim 0.104 \text{ mW m}^{-1} \text{ K}^{-2}$ at 515 K) bulk materials with similar doping levels within the same temperature range.^[12] If oxidation could be reduced, it might be conceivable to surpass such values. Hence, it is achievable to produce high performing n-type SnSe materials in bulk quantities via energy-efficient, sustainable methods (Figure S25). In principle, it should be possible to produce new co-doped SnSe nanomaterials controllably (e.g. with both Bi- and Cl-dopants among others) with only minor adaptations to the present synthesis method.

Preliminary thermal conductivity measurements (κ) performed on **1** and **4** along the direction parallel to pressing

(Figure S26) are also encouraging. κ for **1** (**4**) decreases from ~ 0.89 (~ 0.72) $\text{W m}^{-1} \text{K}^{-1}$ at 300 K to ~ 0.62 (~ 0.40) $\text{W m}^{-1} \text{K}^{-1}$ at 540 K. The higher κ for **1** could be due to its higher percentage of more thermally conductive SnO_2 . However, κ values for both **1** and **4** are still relatively low compared to other examples of n-type polycrystalline SnSe and to p-type single crystals (Figure S26d,e respectively). This could be due to enhanced phonon scattering either from the SnO_2 nano-inclusions in these materials or as a result of the nanostructuring of SnSe itself.

In summary, a simple, quick, low-cost solution synthesis produces Cl-containing SnSe nanoparticles in gram quantities (> 10 g per run for a 2 h growth). Such nanoparticles have been consolidated into n-type Cl-doped SnSe nanostructured pellets, whose thermoelectric power factors can be significantly improved by optimising the Cl doping level. This study not only provides a convenient method for the large-scale synthesis of SnSe nanostructures, but also demonstrates a facile and reliable route to engineer n-type SnSe with well-defined doping concentration. Considering also that p-type SnSe can be synthesised by a very similar method,^[11d] the way is clear towards a unified, cost-effective processing route to large quantities of both the constituent materials needed for a thermoelectric device.

Experimental Section

Full experimental details are provided in the supporting information.

Materials Synthesis. 260 mmol citric acid and 10 mmol $\text{SnCl}_2 \cdot 2\text{H}_2\text{O}$ were added into 50 ml deionised water (DIW) to yield a transparent solution that was heated to boil. 50 ml of freshly prepared $\text{NaHSe}_{(\text{aq})}$ was promptly injected into the boiling solution. The solution was boiled for 2 h and cooled to room temperature under $\text{Ar}_{(\text{g})}$ on a Schlenk line. The products were washed with DIW and ethanol and dried at 50 °C for 12 h. Scaled-up syntheses were performed with 5.5-fold precursor concentrations. The yield is 96(1)% of theoretical production. To tune the particle size and Cl level, samples synthesised over 1 min, 5 min or 24 h durations were also prepared. For the surfactant-free synthesis, 4 ml hydrochloric acid was introduced into SnCl_2 solution in place of citric acid. Pellets were pressed in a graphite die under Ar (uniaxial pressure of ~ 60 MPa; 500 °C; 20 min).

Materials Characterisation and Testing. PXD data were recorded by a PANalytical X'pert Pro MPD diffractometer in Bragg-Brentano geometry (Cu $\text{K}\alpha_1$ radiation, $\lambda = 1.5406$ Å). Rietveld refinement was performed against PXD data using the GSAS and EXPGUI software packages.^[21] Imaging and elemental analysis were performed by SEM (Carl Zeiss Sigma, at 5 and 20 kV respectively) equipped with EDS (Oxford Instruments X-Max 80). Further imaging, elemental analysis and SAED were conducted by TEM (FEI Titan Themis 200 and JEOL JEM-2011, operated at 200 kV). Optical bandgaps were measured by DR-UV-Vis spectroscopy (Shimadzu, UV-2600). The Seebeck coefficient and electrical conductivity of pellets were measured using a Linseis LSR-3 instrument from 300 to 540 K. Thermal diffusivity (D) of pellets was measured using a Linseis LFA 1000 instrument within the same temperature range and thermal conductivity (κ) was calculated using $\kappa = DC_p\rho$, where C_p and ρ are specific heat capacity and density, respectively. Hall measurements were performed on a nanometrics HL5500 Hall system using a Van der Pauw configuration. The XPS experiments were performed using a Kratos Axis Ultra-DLD photoelectron spectrometer with an Al monochromatic X-ray source.

Acknowledgements

This work was financially supported by the EPSRC (EP/K022156/1). The authors thank Mr Peter Chung for assistance with SEM. SRP and JWGB acknowledge the EPSRC for support (EP/N01717X/1). HFG and WZ acknowledge the EPSRC for the Equipment Grant to purchase Titan Themis 200 microscope (EP/L017008/1).

Keywords: Tin selenide • Synthesis • n-type • Thermoelectrics • Nanomaterials

- [1] a) X. F. Duan, Y. Huang, Y. Cui, J. F. Wang, C. M. Lieber, *Nature* **2001**, *409*, 66-69; b) S. J. Oh, C. Uswachoke, T. S. Zhao, J. H. Choi, B. T. Diroll, C. B. Murray, C. R. Kagan, *ACS Nano* **2015**, *9*, 7536-7544.
- [2] D. Zhitomirsky, M. Furukawa, J. Tang, P. Stadler, S. Hoogland, O. Voznyy, H. Liu, E. H. Sargent, *Adv. Mater.* **2012**, *24*, 6181-6185.
- [3] a) J.-S. Rhyee, K. Ahn, K. H. Lee, H. S. Ji, J.-H. Shim, *Adv. Mater.* **2011**, *23*, 2191-2194; b) G. Han, Z.-G. Chen, J. Drennan, J. Zou, *Small* **2014**, *10*, 2747-2765.
- [4] a) L. D. Zhao, S. H. Lo, J. Q. He, H. Li, K. Biswas, J. Androulakis, C. I. Wu, T. P. Hogan, D. Y. Chung, V. P. Dravid, M. G. Kanatzidis, *J. Am. Chem. Soc.* **2011**, *133*, 20476-20487; b) Q. Zhang, Y. C. Lan, S. L. Yang, F. Cao, M. L. Yao, C. Opeil, D. Broido, G. Chen, Z. F. Ren, *Nano Energy* **2013**, *2*, 1121-1127; c) H. Wang, Y. Z. Pei, A. D. LaLonde, G. J. Snyder, *Proc. Natl. Acad. Sci.* **2012**, *109*, 9705-9709; d) A. D. LaLonde, Y. Z. Pei, G. J. Snyder, *Energy Environ. Sci.* **2011**, *4*, 2090-2096.
- [5] H. Fang, Z. Luo, H. Yang, Y. Wu, *Nano Lett.* **2014**, *14*, 1153-1157.
- [6] J. Tang, K. W. Kemp, S. Hoogland, K. S. Jeong, H. Liu, L. Levina, M. Furukawa, X. H. Wang, R. Debnath, D. K. Cha, K. W. Chou, A. Fischer, A. Amassian, J. B. Asbury, E. H. Sargent, *Nat. Mater.* **2011**, *10*, 765-771.
- [7] a) J. B. Zhang, J. B. Gao, E. M. Miller, J. M. Luther, M. C. Beard, *ACS Nano* **2014**, *8*, 614-622; b) Z. Zhang, C. Liu, X. J. Zhao, *J. Phys. Chem. C* **2015**, *119*, 5626-5632.
- [8] a) M. Ibañez, R. J. Korkosz, Z. S. Luo, P. Riba, D. Cadavid, S. Ortega, A. Cabot, M. G. Kanatzidis, *J. Am. Chem. Soc.* **2015**, *137*, 4046-4049; b) D. James, X. Lu, A. C. Nguyen, D. Morelli, S. L. Brock, *J. Phys. Chem. C* **2015**, *119*, 4635-4644.
- [9] a) G. J. Tan, L. D. Zhao, M. G. Kanatzidis, *Chem. Rev.* **2016**, *116*, 12123-12149; b) W. G. Zeier, A. Zevalkink, Z. M. Gibbs, G. Hautier, M. G. Kanatzidis, G. J. Snyder, *Angew. Chem. Int. Ed.* **2016**, *55*, 6826-6841; c) G. J. Snyder, E. S. Toberer, *Nat. Mater.* **2008**, *7*, 105-114.
- [10] a) L. D. Zhao, S. H. Lo, Y. S. Zhang, H. Sun, G. J. Tan, C. Uher, C. Wolverton, V. P. Dravid, M. G. Kanatzidis, *Nature* **2014**, *508*, 373-377; b) L.-D. Zhao, G. Tan, S. Hao, J. He, Y. Pei, H. Chi, H. Wang, S. Gong, H. Xu, V. P. Dravid, C. Uher, G. J. Snyder, C. Wolverton, M. G. Kanatzidis, *Science* **2015**, *351*, 141-144; c) K. Peng, X. Lu, H. Zhan, S. Hui, X. Tang, G. Wang, J. Dai, C. Uher, G. Wang, X. Zhou, *Energy Environ. Sci.* **2016**, *9*, 454-460.
- [11] a) E. K. Chere, Q. Zhang, K. Dahal, F. Cao, J. Mao, Z. Ren, *J. Mater. Chem. A* **2016**, *4*, 1848-1854; b) T.-R. Wei, G. Tan, X. Zhang, C.-F. Wu, J.-F. Li, V. P. Dravid, G. J. Snyder, M. G. Kanatzidis, *J. Am. Chem. Soc.* **2016**, *138*, 8875-8882; c) C. L. Chen, H. Wang, Y. Y. Chen, T. Day, G. J. Snyder, *J. Mater. Chem. A* **2014**, *2*, 11171-11176; d) G. Han, S. R. Popuri, H. F. Greer, J. W. G. Bos, W. Z. Zhou, A. R. Knox, A. Montecucco, J. Siviter, E. A. Man, M. Macauley, D. J. Paul, W. G. Li, M. C. Paul, M. Gao, T. Sweet, R. Freer, F. Azough, H. Baig, N. Sellami, T. K. Mallick, D. H. Gregory, *Angew. Chem. Int. Ed.* **2016**, *55*, 6433-6437; e) S. R. Popuri, M. Pollet, R. Decourt, F. D. Morrison, N. S. Bennett, J. W. G. Bos, *J. Mater. Chem. C* **2016**, *4*, 1685-1691; f) Y.-X. Chen, Z.-H. Ge, M. Yin, D. Feng, X.-Q. Huang, W. Zhao, J. He, *Adv. Funct. Mater.* **2016**, *26*, 6836-6845.
- [12] a) Q. Zhang, E. K. Chere, J. Y. Sun, F. Cao, K. Dahal, S. Chen, G. Chen, Z. F. Ren, *Adv. Energy Mater.* **2015**, *5*, 1500360; b) X. Wang, J. T. Xu, G. Q. Liu, Y. J. Fu, Z. Liu, X. J. Tan, H. Z. Shao, H. C. Jiang, T. Y. Tan, J. Jiang, *Appl. Phys. Lett.* **2016**, *108*, 083902.
- [13] PDF-2 Release 2008, Joint Committee on Powder Diffraction Standards (JCPDS)-International Centre for Diffraction Data (ICDD), **2008**.
- [14] D. D. Vaughn, S. I. In, R. E. Schaak, *ACS Nano* **2011**, *5*, 8852-8860.
- [15] B. Z. Sun, Z. J. Ma, C. He, K. C. Wu, *Phys. Chem. Chem. Phys.* **2015**, *17*, 29844-29853.
- [16] S. I. Kim, S. Hwang, S. Y. Kim, W. J. Lee, D. W. Jung, K. S. Moon, H. J. Park, Y. J. Cho, Y. H. Cho, J. H. Kim, D. J. Yun, K. H. Lee, I. T. Han, K. Lee, Y. Sohn, *Sci. Rep.* **2016**, *6*, 19733.
- [17] D. Feng, Z.-H. Ge, D. Wu, Y.-X. Chen, T. Wu, J. Li, J. He, *Phys. Chem. Chem. Phys.* **2016**.
- [18] a) T. T. X. Vo, T. N. H. Le, Q. N. Pham, C. B. Byl, D. Dragoie, M. G. Barthes-Labrousse, D. Berardan, N. Dragoie, *Phys. Status Solidi A* **2015**, *212*, 2776-2784; b) K. Rubenis, S. Populoh, P. Thiel, S. Yoon, U. Müller, J. Locs, *J. Alloy. Compd.* **2017**, *692*, 515-521.

[19] D. Martinez-Escobar, M. Ramachandran, A. Sanchez-Juarez, J. S. N. Rios, *Thin Solid Films* **2013**, 535, 390-393.

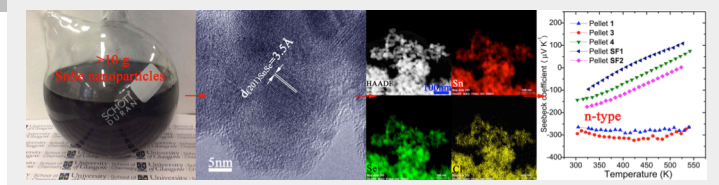
[20] S. Saha, A. Banik, K. Biswas, *Chem. Eur. J.* **2016**, 22, 15634-15638.

[21] a) A. C. Larson, R. B. Von Dreele, General Structure Analysis System (GSAS); Los Alamos National Laboratory Report LAUR 86-748; Los Alamos National Laboratory, **1994**; b) B. H. Toby, *J. Appl. Crystallogr.* **2001**, 34, 210-213.

WILEY-VCH

The Table of Contents

COMMUNICATION



Guang Han,^a Srinivas R. Popuri,^b
Heather F. Greer,^c Lourdes F. Llin,^d Jan-
Willem G. Bos,^b Wuzong Zhou,^c Douglas
J. Paul,^d, Duncan H. Gregory^{a*}

Page No. – Page No.

**Chlorine-Enabled Electron Doping in
Solution-Synthesised SnSe
Thermoelectric Nanomaterials**

An aqueous solution method has been developed for the scalable synthesis of Cl-containing SnSe nanoparticles with tuneable particle size and Cl concentration. Hot pressing produces n-type Cl-doped SnSe nanostructured compacts with thermoelectric power factors optimised *via* control of Cl dopant concentration.